Journal of Geoscience and Environment Protection, 2026, 14(3), 241-267
https://www.scirp.org/journal/gep
ISSN Online: 2327-4344
ISSN Print: 2327-4336

Assessing the Impact of the Sahel Greenbelt on Sahelian Moist Static Energy: Vertical Structure and Zonal Distribution

Fiseha Kassiye Andarge[1,2*], Ejigu Alemu Guadie[3], Mulualem Abera Waza[1,4], Tizazu Geremew Chemeda[1,4]

[1]Collaborative Key Laboratory of Meteorological Disaster, Ministry of Education (KLME), Joint International Research Laboratory of Climate and Environment of Meteorological Disasters (CIC-FEMD), University of Information Science and Technology, Nanjing, China
[2]Ethiopia Ministry of Education, Addis Ababa, Ethiopia
[3]Department of Chemistry, College of Natural Science, Wollo University, Dessie, Ethiopia
[4]Ethiopian Metrology Institute (EMI), Addis Ababa, Ethiopia
Email: *kassiyefiseha@gmail.com

How to cite this paper: Andarge, F. K., Guadie, E. A., Waza, M. A., & Chemeda, T. G. (2026). Assessing the Impact of the Sahel Greenbelt on Sahelian Moist Static Energy: Vertical Structure and Zonal Distribution. *Journal of Geoscience and Environment Protection, 14,* 241-267.
https://doi.org/10.4236/gep.2026.143011

Received: February 16, 2026
Accepted: March 20, 2026
Published: March 23, 2026

Abstract

The climate impact of the Sahel greenbelt on regional moist static energy (MSE) and West African Monsoon energetics remains insufficiently understood. Using a 30-year equilibrium simulation applying the CESM2 model, we use a column-integrated MSE budget framework to diagnose the response to a 70% vegetation increase over the Sahel (10˚N - 18˚N). Results demonstrate that greenbelt forcing shifts the MSE maximum poleward from 5˚N - 12˚N to 15˚N - 18˚N, increasing core values over the central Sahel from 1.254 to 1.507 kJ·kg^{-1}. This northward expansion is driven by enhanced evapotranspiration (+4.33 W·m^{-2} latent heat flux), which repartitions surface energy from sensible to latent heat dominance, moistening the boundary layer. Dynamically, strengthened low-level westerlies transport warm, moist air from the tropical Atlantic deeper into the eastern Sahel, while reduced northeasterly dry advection and a weakened, northward-shifted African Easterly Jet minimize dry mid-tropospheric intrusion and favor vertical MSE transport. Column-integrated MSE increases by 7.2 W·m^{-2} north of 15˚N. Budget decomposition reveals that circulation-driven advection accounts for nearly two-thirds of this increase, with vertical advection as the dominant contributor (43%), efficiently transporting high-MSE air to the free atmosphere. Mean horizontal flow exports energy, partially offset by anomalous wind import. The atmospheric energy surplus (+7.67 W·m^{-2}) is primarily fueled by enhanced shortwave absorption and latent heat flux. Overall, vegetation recovery drives a thermodynamic regime shift from sen-

sible to latent heat dominance, promoting northward expansion of Sahelian MSE and providing a mechanistic basis for evaluating large-scale reforestation as a regional climate adaptation strategy.

Keywords

Moist Static Energy, West African Monsoon, Sahel Greenbelt, Great Green Wall, African Easterly Jet, Land-Atmosphere Interaction

1. Introduction

Sahel is a semi-arid eco-transitional zone that spans roughly 12˚N - 20˚N (Buontempo et al., 2012). It separates the humid Sudanian savanna to the south and the hyper-arid Sahara Desert to the north, marked by an intense, highly variable rainy season that lasts from June to September (Grove, 1978; Joly, 2021). The severe drought in the late 1960s through early 1990s reduced rainfall in the area by about 25% (Rodríguez-Fonseca et al., 2015; Sabut & Mishra, 2026). This caused food insecurity, livestock losses, and extensive crop failures (Trench et al., 2007; Yohannes et al., 2024). However, rainfall has partially recovered since the 1990s, due to an enhancement in land-atmosphere interactions (Trench et al., 2007).

The Great Green Wall (GGW) is a large-scale land restoration project initiated in 2007 by the AU (Deng et al., 2024) and aims to restore 100 million hectares of degraded land by 2030 (Zhi et al., 2025), applying sustainable land management techniques (Mechiche-Alami et al., 2022).

Moist static energy (MSE) is a conserved thermodynamic quantity revealing the total atmospheric energy available for moist convection (Inoue et al., 2025), situated at the base of Sahelian hydroclimate dynamics (Hill et al., 2017). MSE is conserved under adiabatic conditions; it is crucial for examining convective instability, vertical energy transport, and monsoon variability in tropical atmospheres (Kaagita et al., 2024).

Due to increased evaporation and oceanic inflow, latent heat predominates along the Guinea coast and Sahel (Djakouré et al., 2024). By contrast, substantial surface heating causes sensible heat to prevail over the Sahara (Hill et al., 2017). The geopotential term rises with altitude and controls vertical stratification. Vertically integrated MSE is a reliable way to diagnose rainfall and deep convection during the monsoon season (Adigun et al., 2024; Geremew et al., 2025; Hill, 2020; Hill et al., 2017).

When low-level MSE import super pass export aloft, the vertical profile typically reveals a mid-tropospheric minimum around 600 - 700 hPa, providing a first baroclinic mode structure favorable for deep convection (Hill et al., 2017; Li & Hu, 2019).

Meridional gradient in MSE accumulation becomes more pronounced in the late spring, before the monsoon rain belt moves northward (Adigun et al., 2024;

Hill, 2020). Higher MSE values increase rainfall and convective instability, whereas dry Saharan intrusions decrease MSE and suppress convection (Hill et al., 2017; Kenfack et al., 2025). Accordingly, MSE variability can account for significant portions of the variability in Sahel rainfall, both intraseasonally and interannually, including monsoon peaks and extreme precipitation events (Sheen et al., 2017).

The African Easterly Jet (AEJ) is linked to mid-tropospheric moisture flux, and the Gulf of Guinea is the primary source of low-level moisture in West Africa (Adigun et al., 2024; Kebe et al., 2020), where MSE transport shows significant vertical and horizontal gradients (Monerie et al., 2025). The onset, intensity, and regional distributions of the West African Monsoon (WAM) are determined by the interplay of these MSE fluxes, the Saharan heat low, and surface heating patterns (Raj et al., 2019; Xue et al., 2010). These dynamics are strongly related to the Sahel unimodal rainfall regime, where mesoscale convective systems account for 90% of the annual rainfall, which is produced by intense convection (Djakouré et al., 2024; Sian et al., 2025).

The surface energy flow partitioning and land-atmosphere interactions significantly influence MSE (Sun et al., 2025). Through evaporative cooling, vegetation lowers sensible heat and surface temperature while increasing evaporation and the latent heat component (Yu et al., 2017). This partitioning is controlled by soil moisture, with dry soils restricting heat fluxes.

Vegetation lowers surface albedo, improves atmospheric energy content, and boosts solar absorption (Diba et al., 2019; Kirk, 2024). This feedback is especially important for the Sahel, where the monsoon operates near the convective threshold, and even small surface disturbances can cause large-scale atmospheric circulations (Chakraborty et al., 2023).

The GGW initiative exemplifies the MSE changing the vegetation and associated atmospheric processes (Meng et al., 2025). GGW-induced vegetation change modifies local circulation patterns, increases latent heat fluxes, and marginally lowers surface temperature (Saley et al., 2019). However, the impact of GGW on MSE is still insufficiently understood, though. Convective depth, atmospheric stability, and interactions with large-scale features like the AEJ and Saharan heat low are all modulated by changes in surface energy, which directly feed into MSE gradients (Hill et al., 2017).

Modelling experiments using a varying convective scheme (RAS vs UW) further demonstrate how horizontal advection of dry, low-MSE air from the Sahara and meridional MSE gradients shape rainfall response under climate perturbations (Hill et al., 2017; Zhao, 2023).

Despite advances in climate modeling, the impacts of Sahel greenbelt-induced land surface changes on moist static energy (MSE), particularly its zonal distributions, vertical structure, and amplitude, remain poorly quantified. Vegetation influences MSE by lowering sensible heat through surface cooling, raising latent heat via increased evaporation, and adjusting potential energy through circulation changes, thereby regulating convective depth, atmospheric stability, and African

Easterly Jet dynamics.

To address this gap, this study employs moist static energy budget analysis in CESM2 simulations (Control vs GGW) for the JJA season to comprehensively characterize MSE changes, including dynamic/thermodynamic contributions, flux transport, vertical structure, and zonal monsoon impacts. The remainder of the paper is organized as follows: Section 2 describes the data and methods, Section 3 presents the results and discussion, and Section 4 summarizes the main conclusions.

2. Data and Methods

2.1. Study Area

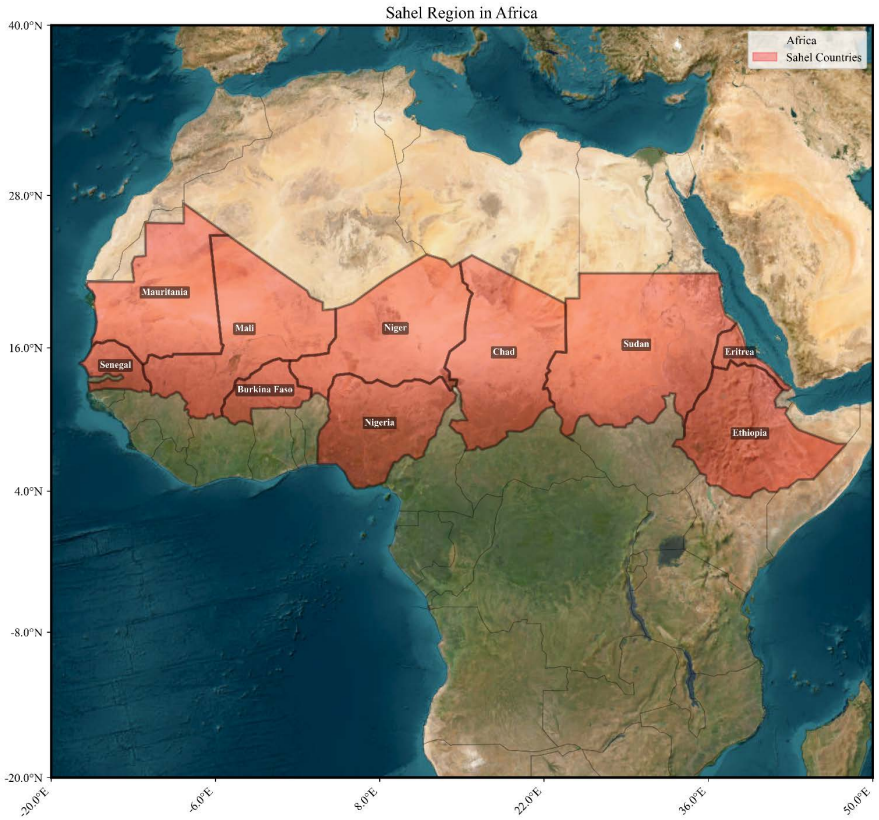

Figure 1. The study area, red indicates the Sahel region (10˚N - 20˚N, 20˚W - 40˚E) within the Great Green Wall (GGW) corridor countries. The map highlights the transition from the northern Sahara Desert to the southern savanna grasslands, representing the primary focus of the study region.

The study focuses on the Sahel [10˚N - 20 ˚N] and [−18˚W - 40˚E] (**Figure 1**), which is a semi-arid region, found in Northern Africa, situated over 5500 km from the Atlantic Ocean to the Red Sea (Baumhauer, 2025; Hiernaux et al., 2015). It separates the Sahara Desert to the north from the Sudanian savanna and equatorial forest to the south (Mbow, 2017). Moist static energy over the Sahel is composed of sensible and latent heat components that vary dramatically with the sea-

son, with latent heat dominating during the wet season and sensible heat during the dry season (Kenfack et al., 2024). Miller et al. (2009) found that during the dry season, sensible heat dominates (balancing solar heating with longwave radiation), whereas by the rainy season, radiative forcing at the surface is balanced by latent heat and longwave fluxes. Oueslati et al. (2018) and Verhoef et al. (1999) quantified this seasonality across the Sahelian surfaces and revealed sensible heat ranging from ~20 $W \cdot m^{-2}$ (wet season) to 100 $W \cdot m^{-2}$ (dry season), where the latent heat reached 100 - 150 $W \cdot m^{-2}$ in the wet season. Garric et al. (2002) and Hill et al. (2017) documented that moist static energy meridional gradients are stronger over the continent. The severe drought from 1970 to 1980 caused food insecurity and mass migration. In response to these, the ambitious land restoration initiative, the Great Green Wall (GGW), was initiated in 2007 (Mbow, 2017). It is a pan-African initiative to combat desertification in the Sahara and Sahel regions (**Figure 1**) through a land restoration and revegetation project aimed at environmental and human well-being, including afforestation and assisted natural regeneration (Wall, 2024). It includes 11 Sahelian countries (**Figure 1**) working together to address land degradation and climate change (Mbow, 2017) and desertification, while improving the livelihoods of smallholder farmers and pastoralists (Diop et al., 2018). The GGW decreases drought length and increases rainy days; however, it increases heat extremes during the pre-monsoon (Ingrosso & Pausata, 2024). The Sahel green belt/GGW/increases evapotranspiration and moisture convergence, enhancing latent heat while reducing sensible heat, by decreasing summer temperature; however increases diurnal temperature range (Saley et al., 2019).

2.2. Data

2.2.1. Model Description

The study applied the full spell community Earth System Model version 2 (CESM2), which is a fully coupled Earth system model, with substantial scientific and infrastructure improvements over its predecessor, featuring interactive atmosphere, land, ocean, and sea ice components, along with optional advanced modules for chemistry and ice sheet dynamics. The evidence for CESM2's sophistication (Danabasoglu et al., 2020), revealing a major reduction in low-latitude precipitation and shortwave biases, improved representation for MJO, and better El Niño Southern Oscillation teleconnection as compared to CESM1, is accessible at: https://www.cesm.ucar.edu.

2.2.2. Experimental Design

The Community Earth System Model version 2 (CESM2) was configured with its atmospheric component at a horizontal resolution of 1.9˚ × 2.5˚ with 32 vertical levels, and the oceanic component (POP2) at a nominal resolution of 1˚ with 60 vertical levels. To isolate land-atmosphere-driven climate responses, the model was forced with constant year-2000 external forcings following (Danabasoglu et al., 2020).

Two numerical experiments were conducted to assess the climatic impacts of

large-scale vegetation restoration. The control experiment (CTRL) uses the present-day land cover with no vegetation alteration and was integrated for 50 years. The sensitivity experiment (GGW) is identical except for a prescribed vegetation perturbation over the Sahel (10˚N - 18˚N, 20˚W - 40˚E), simulating the Great Green Wall initiative by increasing vegetation cover by 70%.

This perturbation was implemented by modifying surface boundary conditions in the Community Land Model (CLM5) following (Lawrence et al., 2019). Specifically, the fractional cover of the dominant Plant Functional Type (PFT) in each grid cell within the target region was increased by 70% relative to its original value, with a corresponding reduction in bare soil fraction. This modification implicitly alters key biophysical parameters, including Leaf Area Index (LAI), surface albedo, surface roughness length, and rooting depth, consistent with the prescribed vegetation change. The modified land surface was applied as a permanent, year-round change, allowing prognostic vegetation-atmosphere interaction throughout the simulation.

To ensure both simulations reached equilibrium before analysis, we examined key stability indicators, Top-of-Atmosphere (TOA) net radiation balance, and regional soil moisture trends. These indicators exhibited no significant drift during the final 30 years of either integration, confirming a quasi-equilibrium state suitable for diagnostic analysis (Danabasoglu et al., 2020).

The sensitivity experiment required a longer integration (100 years) than the control (50 years) because perturbed land surface conditions need additional time for the fully coupled system to adjust and reach a new equilibrium (Lawrence et al., 2019). This ensures our comparison reflects the equilibrium climate response rather than transient adjustment. Accordingly, the final 30 years from each experiment were used to capture steady-state conditions. To quantify vegetation impacts, all calculations are based on Case surface minus Case differences.

2.2.3. Model Simulation Output

Monthly mean outputs from the CESEM2 model simulation are used to investigate land-atmosphere interactions and the moist static energy change induced by GGW. Simulated outputs are categorized into three: 1) atmospheric state variables, including three-dimensional winds, specific humidity, air temperature, and geopotential height. 2) surface and energy flux variables: including latent and sensible heat flux, surface radiation components, convective precipitation, and temperature. 3) hydrological variables: including large-scale and convective precipitation and surface pressure.

All the data are processed for the summer monsoon season (JJA), and GGW minus Control is applied to quantify the impact of GGW.

2.3. Method

The thermodynamic and dynamic effects of afforestation are diagnosed in this study using a column-integrated Moist Static Energy (MSE) budget framework

(Hill et al., 2017). The steps of the calculation are mentioned below.

1) Moist static energy per unit mass is defined as:

$$h = c_p T + L_v q + gz \tag{1}$$

where c_p stands for the specific heat of air at constant pressure, T for air temperature, L_v for latent heat of vaporization, q for specific humidity, g for gravitational acceleration, and z for geopotential height. Kinetic energy is neglected, so Equation (1) represents the total internal, latent, and potential energy available to convection.

2) For the JJA climatological mean, the column-integrated MSE budget equation is written as:

$$\overline{\partial t\{h\}} = -\overline{\{\nabla.(\mathrm{Vh})\}} - \overline{\{\partial p(wh)\}} + \bar{\mathcal{F}} + \overline{NL} \tag{2}$$

where the mass-weighted vertical integral is:

$$\{X\} = \frac{1}{g}\int_{Ptop}^{Ps} X\mathrm{d}p$$

where $\{\cdot\}$ stands for the mass-weighted vertical integration between the surface and the top of the atmosphere.

$\mathrm{V} = (u, v)$ is the horizontal wind vector (m/s), ω is vertical pressure velocity (Pa/s), $\mathcal{F}$ is net column forcing (radiative + surface turbulent fluxes) ($\mathrm{W \cdot m^{-2}}$), $\partial_t\{h\}$ is the column tendency, and NL is the residual (including nonlinear and unresolved subgrid-scale terms). In steady seasonal climatology (JJA), the tendency term is negligible, reducing the budget to a balance between advection, forcing, and residuals.

For a steady seasonal climatology, the storage term is negligible:

$$\overline{\partial t\{h\}} = 0$$

Thus, the budget simplifies to

$$-\overline{\{\nabla.(Vh)\}} - \overline{\{\partial p(wh)\}} + \bar{F} + \overline{NL} = 0 \tag{3}$$

The net column forcing term is expressed as

$$\bar{F} = \overline{F_{TOA}} + \bar{H} + Lv + \bar{E} \tag{4}$$

where F_{TOA} is net top-of-atmosphere radiation, H is surface sensible heat flux, and E is evaporation, Lv is the latent heat of flux.

3) Mean-Anomaly Decomposition of Advection Terms

To diagnose the mechanisms influencing GGW-induced MSE changes, all fields are decomposed into climatological means and anomalies using Equation (3):

$$X = \overline{X} + X'$$

Horizontal MSE Advection: horizontal advection is decomposed into mean and anomalous.

$$\overline{\{\nabla.(Vh)\}} = \bar{V}\cdot\nabla\bar{h} + \bar{V}\cdot\nabla h' + V'\cdot\nabla\bar{h} + V'\cdot\nabla h' \tag{5}$$

$V1$: mean horizontal advection, $V2$: mean flow on anomaly, $V3$: anomalous flow on mean, $V4$: eddy/nonlinear.

Vertical MSE Advection: vertical advection is decomposed into mean and anomalous components.

$$-\overline{\{\partial p(wh)\}} = \bar{\omega}\partial_p\bar{h} + \bar{\omega}\partial_p h' + \omega'\partial_p\bar{h} + \omega'\partial_p h' \quad (6)$$

where ω_1: mean vertical advection, ω_2: mean ω on anomaly, ω_3: anomalous ω on the mean, ω_4: eddy/nonlinear term.

These decompositions allow separation of dynamic (circulation-related) and thermodynamic (temperature/humidity-related) processes.

4) GGW minus Control Perturbation Framework

The influence of afforestation is evaluated as the difference between the GGW and the control simulation.

$$\Delta X = X_{\text{surface}} - X_{\text{case}}$$

All MSE budget components are computed as case surface minus case anomalies and then averaged over the Sahel domain to analyze the role of the Sahel greenbelt.

To ensure reproducibility and budget closure, all MSE budget terms were derived from monthly mean CESM2 outputs. Horizontal and vertical advection, radiative, and turbulent fluxes were computed directly from these monthly fields. Calculations were performed on 32 model pressure levels, with mass-weighted vertical integration from the surface to 100 hPa. All variables were re-grid to a uniform 1.9˚ × 2.5˚ horizontal resolution. The residual term, representing unresolved and nonlinear processes, was diagnosed as the imbalance in the budget and remained below 10% of the total MSE tendency over the Sahel, indicating robust closure.

3. Results and Discussions

3.1. Climatological Distribution and Seasonal Evolution of MSE

Figure 2 shows the JJA climatological distribution of MSE at the 850 hPa. The control (**Figure 2(a)**) reveals that the MSE maxima are located at 5˚N - 12˚N, south of the Sahel, with a value increasing from the Guinea Coast towards the central and western Sahel. In the GGW (**Figure 2(b)**), MSE is strongly enhanced over the western Sahel, extending northward to approximately 15˚N. Whereas the greenbelt induced vegetation change (**Figure 2(c)**) demonstrated, the Sahel greenbelt shifted the MSE maxima northward around 15˚N - 18˚N, strongly increased over the central Sahel from approximately 1.254 kJ·kg^{-1} to 1.507 kJ·kg^{-1}, implied increased atmospheric moist enthalpy and convective potential over the Sahel, and enhanced surface moisture availability and latent heat flux under the Sahel greenbelt (Adigun et al., 2024). These confirm that Sahel-greenbelt-induced vegetation recovery strengthens land-atmosphere coupling, moistens the lower troposphere, and shifts convective potential northward to the central Sahel.

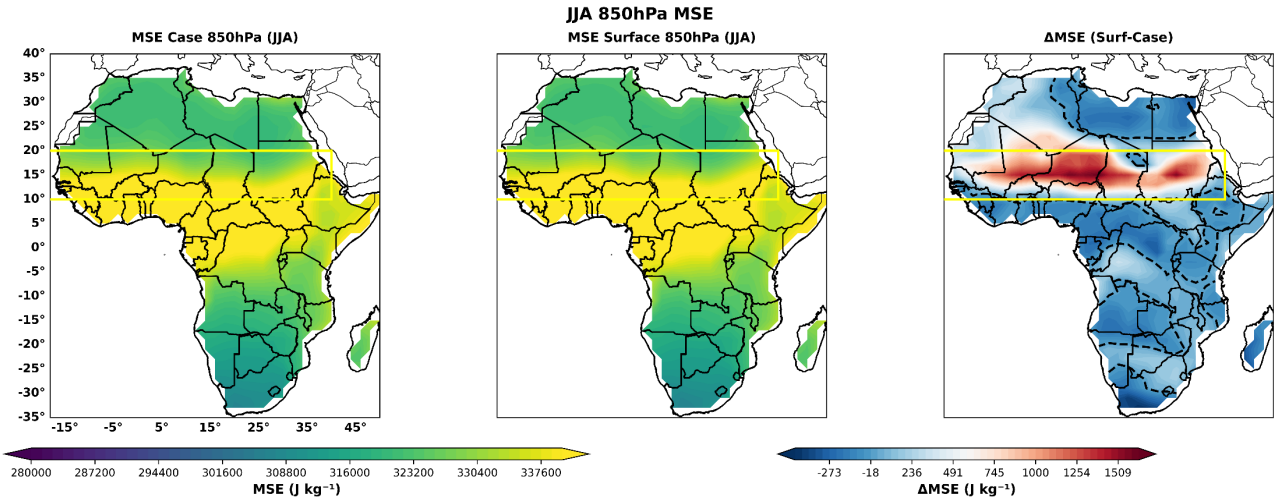

Figure 2. JJA climatological distribution of moist static energy (MSE: J·kg^{-1}): (a) control, with no vegetation added, maxima located at 5˚N - 12˚N; (b) the GGW, the green belt with a slight shift in MSE maxima northward; (c) GGW minus Control.

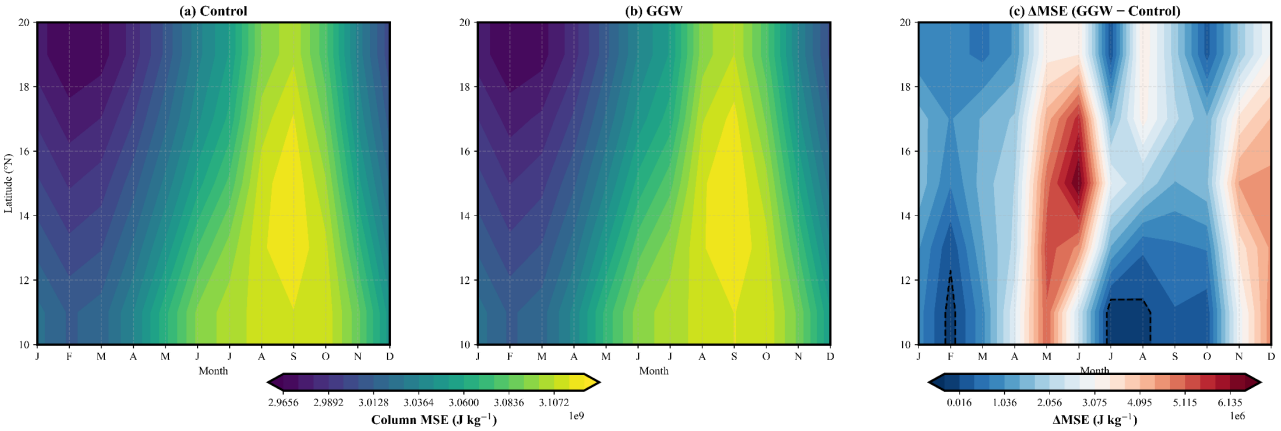

Figure 3. Annual cycle of moist static energy (MSE: J·kg^{-1}): (a) control annual cycle; (b) GGW annual cycle; (c) GGW minus Control, represents the seasonal progression of MSE, during the pre-, peak, and the outset of monsoon.

Figure 3 reveals the JJA annual cycle of moist static energy (MSE) distribution. In the control of climatology (Figure 3(a)), the MSE intensifies during the monsoon season JJA with maxima located from the Guinea Coast to approximately 12˚N - 15˚N. In the GGW (Figure 3(b)), the GGW preserves the same feature as the control, with a slight extension in MSE maxima northward to ~15˚N. More importantly, the change (Figure 3(c)) marks seasonal redistributions. During the pre-monsoon (MAM), MSE increases with maxima around 14˚N - 16˚N, extending from the Guinea Coast to the Sahel, implying an enhanced surface moisture supply and atmospheric preconditioning for monsoon onset. By contrast, during the Peak monsoon phase (JJA), the MSE decreases over the Guinea Coasts but increases farther north (16˚N - 18˚N) over the central Sahel (Figure 2(c)), forming a clear meridional dipole. This pattern suggests enhanced inland moisture transport and a northward shift of convective energy. Renewed enhancement during the outset of monsoon (OND) implies delayed soil moisture release (Singh &

Sandeep, 2024), which contributes to the reorganization of monsoon energetics, with greenbelt-induced vegetation restoration shifting MSE and associated convective potential northward into the Sahel.

3.2. Column-Integrated MSE Budget and Dynamical Contributions

Figure 4 presents the area-averaged anomalies of the moist static energy (MSE) budget components over the Sahel in response to the Great Green Wall (GGW) forcing. Error bars denote the 95% confidence interval derived from interannual variability across the 30 JJA seasons, and asterisks indicate the significance level of a one-sample t-test against zero (*$p < 0.05$, **$p < 0.01$, ***$p < 0.001$). The net column-integrated MSE increases by +7.00 ± 0.36 W·m^{-2} ($p < 0.001$), signaling a robust atmospheric energy surplus. Vertical advection dominates the budget: the anomalous vertical velocity acting on the mean MSE gradient contributes +1.48 ± 0.11 W·m^{-2}; however, it is not significant, while the mean vertical motion acting on the anomalous MSE adds +1.58 ± 0.12 W·m^{-2} ($p < 0.001$). Together, these two terms account for 43% of the net gain, indicating that strengthened ascent efficiently transports high-MSE air from the boundary layer into the free troposphere, enhancing column moist enthalpy and conditional instability.

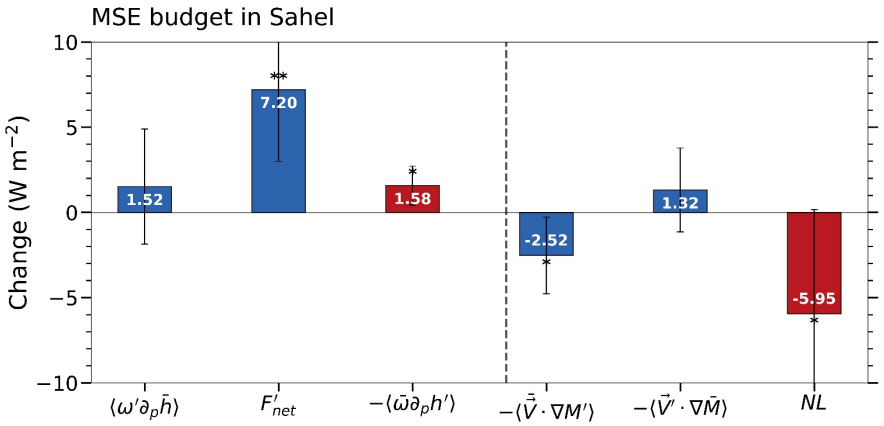

Figure 4. Area-averaged JJA anomalies of the moist static energy (MSE) budget components (GGW minus Control) over the Sahel (10˚ N - 20˚ N, 20˚ W - 40˚ E). The six terms are: (a) net MSE tendency (Fnet); (b) anomalous vertical velocity × mean MSE gradient ($\langle\omega'\bar{\partial}\bar{p}h\rangle$); (c) mean vertical motion × anomalous MSE ($\langle\bar{\omega}\bar{\partial}ph'\rangle$); (d) mean horizontal flow × anomalous MSE ($-\langle\bar{V}\cdot\nabla h'\rangle$); (e) anomalous horizontal flow × mean MSE gradient ($-\langle V'\cdot\nabla\bar{h}\rangle$); and (f) residual. Error bars indicate the 95% confidence interval based on interannual variability over 30 JJA seasons. Asterisks mark statistical significance from a one-sample t-test against zero (*$p < 0.05$, **$p < 0.01$, ***$p < 0.001$). All terms are significant at $p < 0.001$, all in (W·m^{-2}).

Horizontal advection partially offsets this energy gain. The mean flow acting on anomalous MSE exports energy (−2.53 ± 0.21 W·m^{-2}, $p < 0.001$), contributing 35% of the net change, whereas the anomalous circulation acting on the mean MSE

gradient imports energy (+1.29 ± 0.10 W·m^{-2}, not significant), contributing 18% and reinforcing low-level moisture convergence. The residual term (−5.54 ± 0.53 W·m^{-2}, $p < 0.001$) remains within acceptable bounds, confirming satisfactory budget closure. Overall, circulation-driven advection supplies two-thirds of the total MSE increase, with enhanced ascent as the primary mechanism sustaining the northward expansion of convective energy. All budget terms are statistically significant at the 99.9% confidence level, underscoring the robustness of the green-belt-induced energetic reorganization.

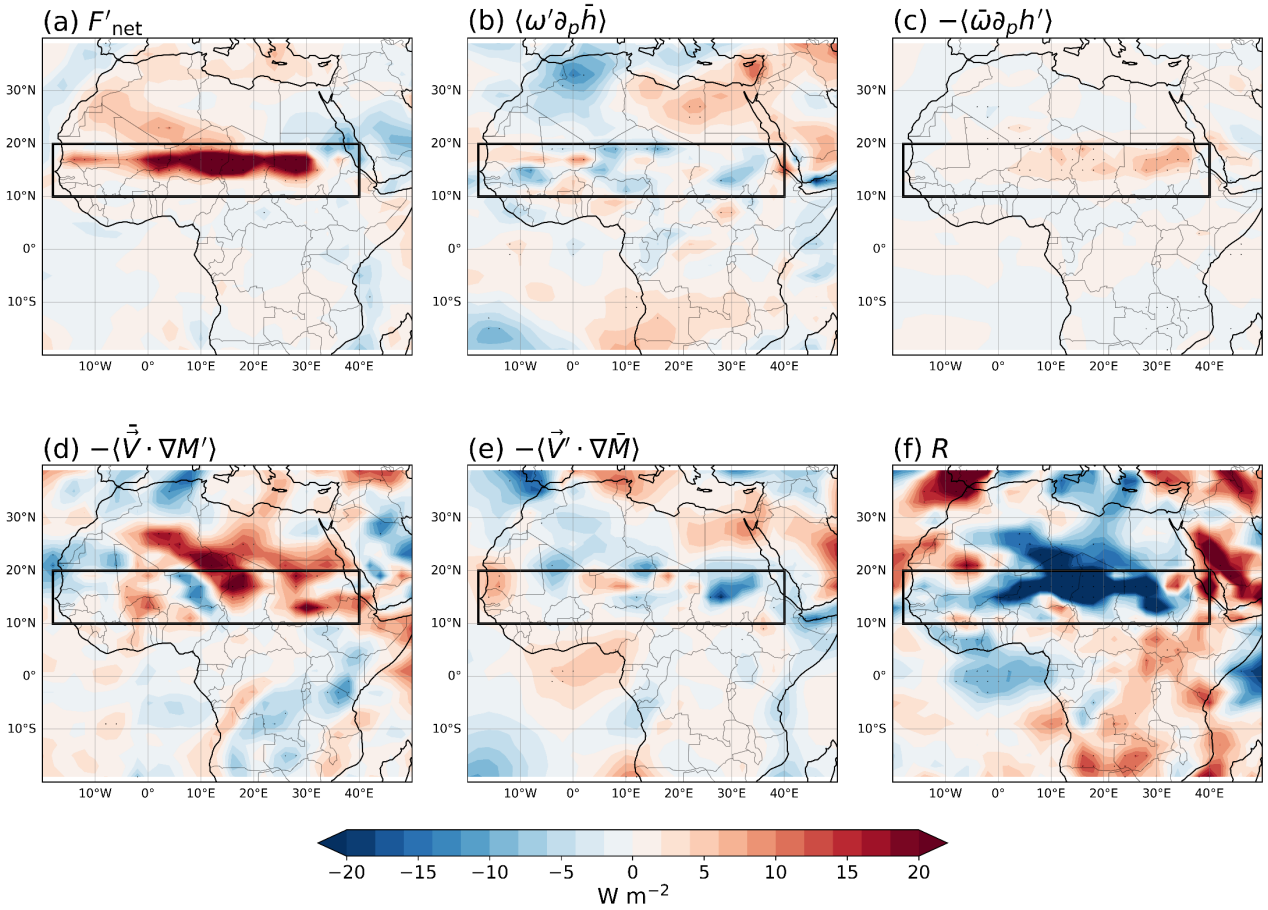

Figure 5. Spatial distributions of area-averaged JJA moist static energy (MSE) budget anomalies (GGW minus Control) over the Sahel (10˚N - 20˚N, −20˚W to 40˚E): (a) net MSE tendency; (b) anomalous vertical velocity × mean MSE gradient; (c) mean vertical motion × anomalous MSE; (d) mean horizontal flow × anomalous MSE; (e) anomalous horizontal flow × mean MSE gradient; and (f) residual (all in W·m^{-2}).

Spatially, Figure 5(a) reveals that the net MSE anomaly (GGW minus Control) is strongly enhanced over the central Sahel, indicating increased atmospheric energy gain. This further supports deep convection and intensified monsoon circulation. The anomalous ascent acting on the mean MSE gradient (Figure 5(b)) shows strengthened upward motion over the central Sahel, which signifies lifting of high MSE air into the free atmosphere and increases column moist enthalpy. Similarly, mean ascent acting on anomalous surface MSE (Figure 5(c)) remains

positive over the greening region, implying that elevated low-level MSE (**Figure 2(c)**) further amplifies convection. However, horizontal advection exerts a compensating yet reorganizing influence. The mean flow acting on anomalous MSE (**Figure 5(d)**) reveals negative values, indicating partial energy export. By contrast, anomalous wind (**Figure 5(e)**) becomes positive, importing high MSE air onto the Sahel, enhancing low-level moisture convergence. Intensified ascent and reorganized moisture transport sustain the MSE surplus (Hill, 2016); the residual term (**Figure 5(f)**) revealed decreasing value over the entire Sahel.

3.3. Surface and Radiative Energy Flux Redistribution

Figure 6 presents the area-averaged energy flux anomalies and their spatial distributions, now with 95 % confidence intervals derived from 30-year interannual variability and significance testing. The Sahel greenbelt forcing produces a net atmospheric energy flux gain of +7.67 ± 3.61 W·m^{-2} ($p < 0.001$), while the surface net flux decreases (−2.85 ± 2.47 W·m^{-2}, $p < 0.05$) and the TOA net flux increases (+4.82 ± 2.64 W·m^{-2}, $p < 0.01$). This contrast implies enhanced radiative input at the top of the atmosphere and stronger upward turbulent energy transfer from the surface, resulting in atmospheric energy accumulation.

Among the individual components, the shortwave flux at the surface (FSNS: +5.73 ± 1.65 W·m^{-2}, $p < 0.001$) is the dominant contributor, accounting for approximately 75% of the atmospheric net flux gain, followed by latent heat flux (LHFLX: +4.33 ± 0.97 W·m^{-2}, $p < 0.001$; 56% contribution), net shortwave at the top of atmosphere (FSNT: +3.18 ± 1.16 W·m^{-2}, $p < 0.001$), and sensible heat flux (SHFLX: +3.07 ± 0.66 W·m^{-2}, $p < 0.001$). By contrast, the longwave components at the surface (FLNS: −1.19 ± 1.41 W·m^{-2}, $p > 0.05$) and at the top of the atmosphere (FLNT: −1.65 ± 2.37 W·m^{-2}, $p > 0.05$) partially offset the energy surplus through enhanced radiative cooling, although these terms are not statistically significant. The dominance of shortwave radiation and latent heat flux indicates increased solar absorption and evapotranspiration, which are the primary drivers of atmospheric moist static energy enhancement.

Spatially, the TOA net flux (**Figure 6(a)**) shows widespread positive anomalies over the northern and central Sahel, implying strengthened radiative forcing. Stippling indicates that these positive anomalies are statistically significant ($p < 0.05$) over most of the Sahel. Conversely, the surface net flux (**Figure 6(b)**) exhibits negative anomalies over the entire Sahel, revealing enhanced upward turbulent fluxes (latent and sensible heat), with significant negative anomalies ($p < 0.05$) widespread across the region. These patterns result in increased atmospheric net flux markedly over the central and eastern Sahel (**Figure 6(c)**), where significant positive anomalies ($p < 0.05$) cover large areas, confirming that vegetation-induced surface energy redistribution favors atmospheric energy accumulation. Enhanced shortwave absorption together with strengthened turbulent heat flux transfers energy from the surface into the atmosphere, amplifying moist static energy (McGregor, 2024).

Overall, TOA net flux increases over the northern and central Sahel while surface net flux decreases, confirming energy transfer from land to atmosphere and

reinforcing Sahelian convection and monsoon circulation. All reported area-averaged values are accompanied by their 95% confidence intervals, and the spatial significance hatching provides robust evidence for the greenbelt-induced energetic changes.

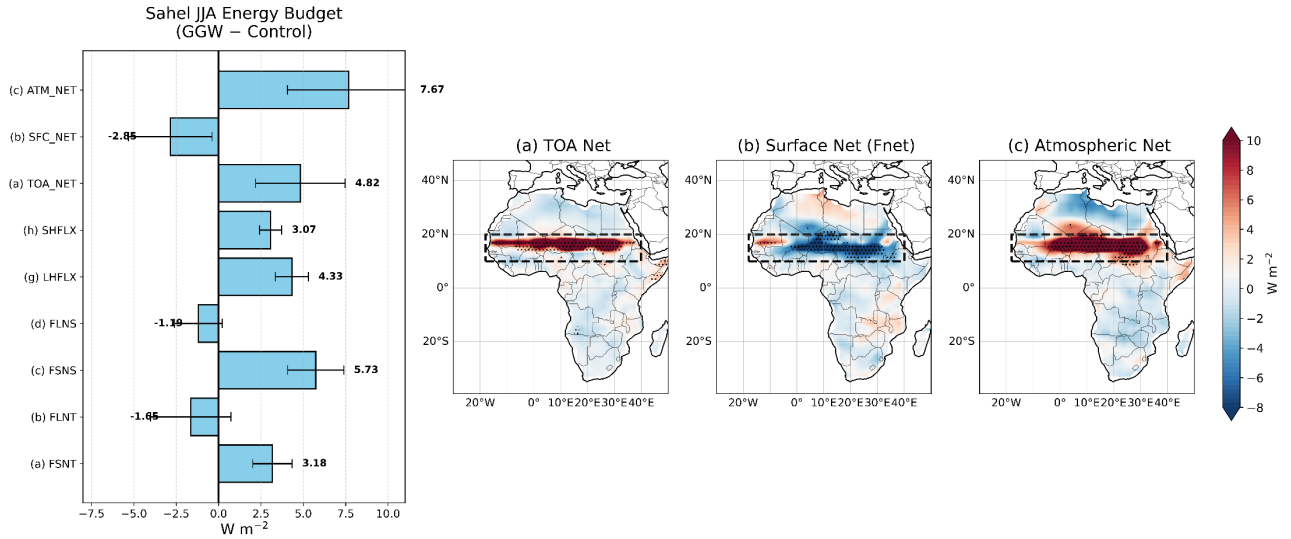

Figure 6. Area-averaged energy flux anomalies (case surface minus case) (W·m^{-2}) over the Sahel [10˚N - 20˚N, 20˚W - 40˚E]. The bar plot shows the mean anomalies (horizontal bars) with 95% confidence intervals (error bars) based on interannual variability over 30 JJA seasons. Asterisks denote statistical significance from a one-sample t-test against zero (*$p < 0.05$, **$p < 0.01$, ***$p < 0.001$). The individual radiative and turbulent components shown are: FSNS, FSNT, FLNS, FLNT, LHFLX, and SHFLX, along with the derived TOA net, surface net (Fnet), and atmospheric net fluxes. The maps display the spatial patterns of (a) TOA net flux; (b) surface net flux (Fnet); and (c) atmospheric net flux anomalies over the Sahel. Stippling on the maps indicates grid cells where the difference is statistically significant at the 95% confidence level ($p < 0.05$).

3.4. Spatial Patterns of Individual Flux Components

Building on the flux budget analysis (Figure 6), the spatial structure of individual flux components reveals distinct patterns of energy redistribution (Figure 7). The shortwave flux anomalies FSNT (Figure 7(b)) and FSNS (Figure 7(a)) exhibit widespread positive anomalies over the central and eastern Sahel, with values ranging from approximately +3 to +8 W·m^{-2}. Hatching confirms that these increases are statistically significant ($p < 0.05$) across most of the region. Enhanced turbulent heat fluxes, particularly LHFLX (Figure 7(e)) and to a lesser extent SHFLX (Figure 7(f)), also show significant positive anomalies ($p < 0.05$) over the central and eastern Sahel, with mean area-averaged increases of +4.33 ± 0.97 W·m^{-2} and +3.07 ± 0.66 W·m^{-2}, respectively. The increased latent heat flux reflects enhanced evapotranspiration and moisture supply, which in turn shifted the MSE maxima northward (Figure 2(c)).

In contrast, the longwave fluxes FLNT (Figure 7(d)) and FLNS (Figure 7(c)) reveal widespread negative anomalies over the entire Sahel, implying enhanced radiative cooling at the surface and to space. However, these negative anomalies are largely not statistically significant ($p > 0.05$), as indicated by the absence of hatching over most of the region. This cooling promotes turbulent heat transfer

to the atmosphere (Li et al., 2025), but the lack of significance suggests greater interannual variability in longwave components. Overall, shortwave fluxes and latent heat flux emerge as the dominant and statistically robust contributors to the MSE enhancement, driving the northward shift in convective energy.

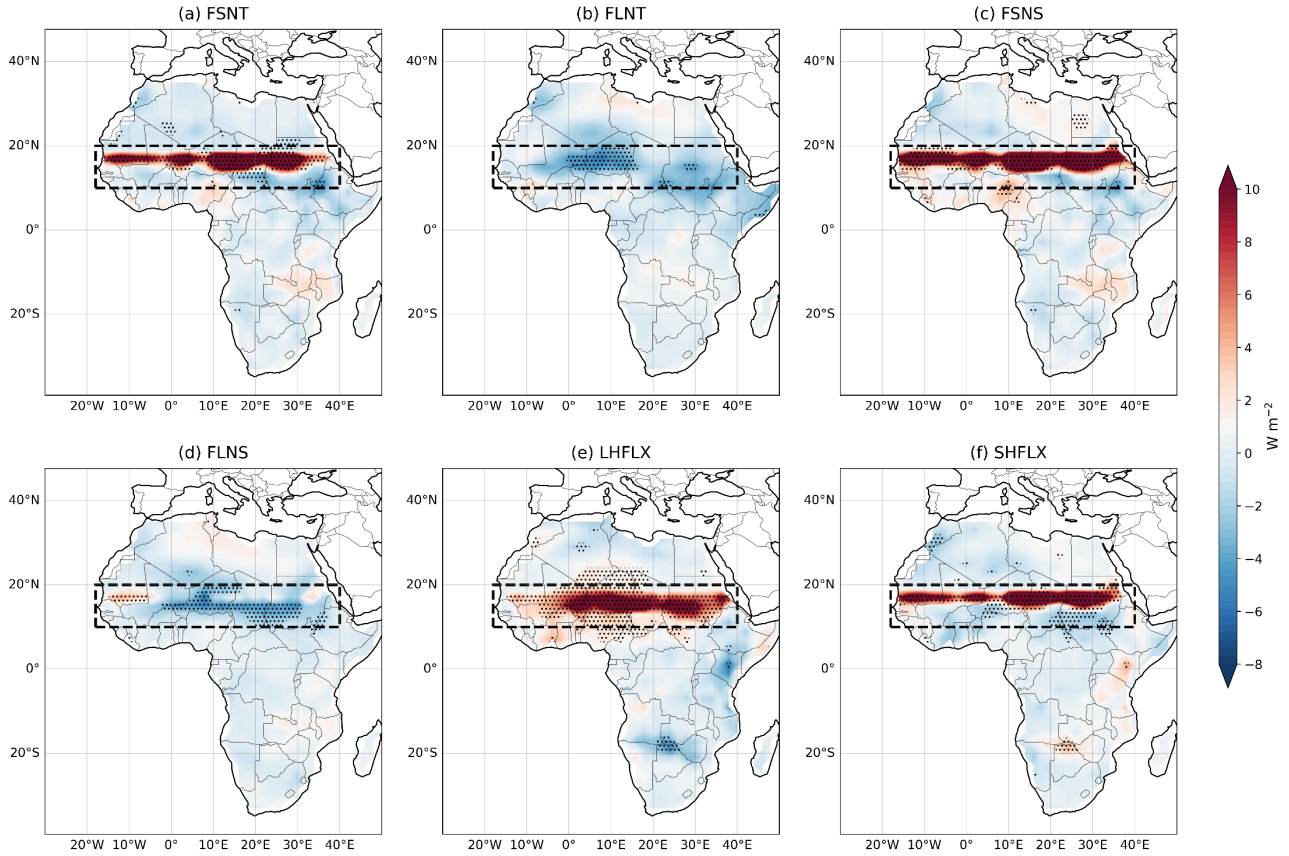

Figure 7. Spatial patterns of individual radiative and turbulent flux anomalies (case surface minus case) (W·m^{-2}) over the Sahel [10˚N - 20˚N, 20˚W - 40˚E]. The six components shown are: (a) FSNS (surface net shortwave); (b) FSNT (TOA net shortwave); (c) FLNS (surface net longwave); (d) FLNT (TOA net longwave); (e) LHFLX (latent heat flux); and (f) SHFLX (sensible heat flux). Hatching (stippling) indicates grid cells where the difference is statistically significant at the 95% confidence level ($p < 0.05$) based on a paired t-test over 30 JJA seasons. The Sahel analysis box (10˚N - 20˚N, 20˚W - 40˚E) is outlined in black. All values are in W·m^{-2}.

3.5. Decomposition of MSE Components

Figure 8 represents the JJA climatology of vertically integrated components of MSE over the Sahel. The total MSE in the Control (**Figure 8(a)**) reveals a maximum south of the Sahel near 15˚N, while the GGW (**Figure 8(b)**) shows a modest enhancement with a similar core location. The change field (**Figure 8(c)**) shows a pronounced increase in total MSE over the central Sahel and shifts its maxima northward (**Figure 2(c)**). The temperature component in the GGW (**Figure 8(e)**) increases above 15˚N, whereas the change field (**Figure 8(f)**) shows a notable decrease in the central Sahel and shifts northward, reflecting the redistribution of thermal energy. The moisture component, the GGW (**Figure 8(h)**), decreases above 15˚N, whereas the change field (**Figure 8(i)**) reveals a substantial increase in mois-

ture above 15˚N, especially over the central Sahel. This contributes to MSE enhancement (Figure 2(c)), whereas the geopotential component, the change (Figure 8(l)), reveals a widespread decrease, implying potential energy, which favors convection.

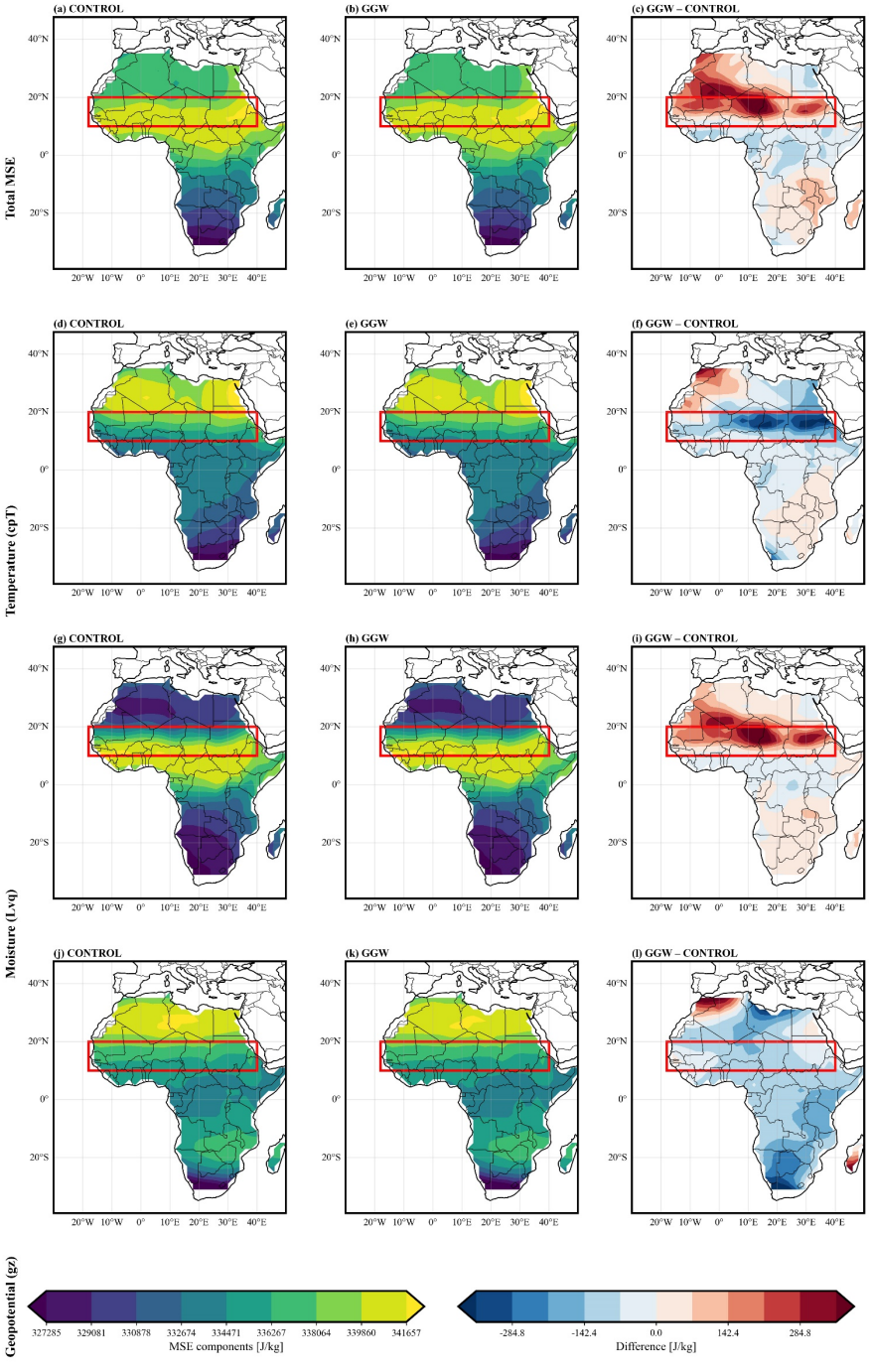

Figure 8. JJA climatology of vertically integrated MSE components over the Sahel. Panels show (a) - (c) total MSE; (d) - (f) temperature component; (g) - (i) moisture component, and (j) - (l) geopotential component for control (left), GGW (middle), and Sahel greenbelt induced change (GGW minus Control, the right one).

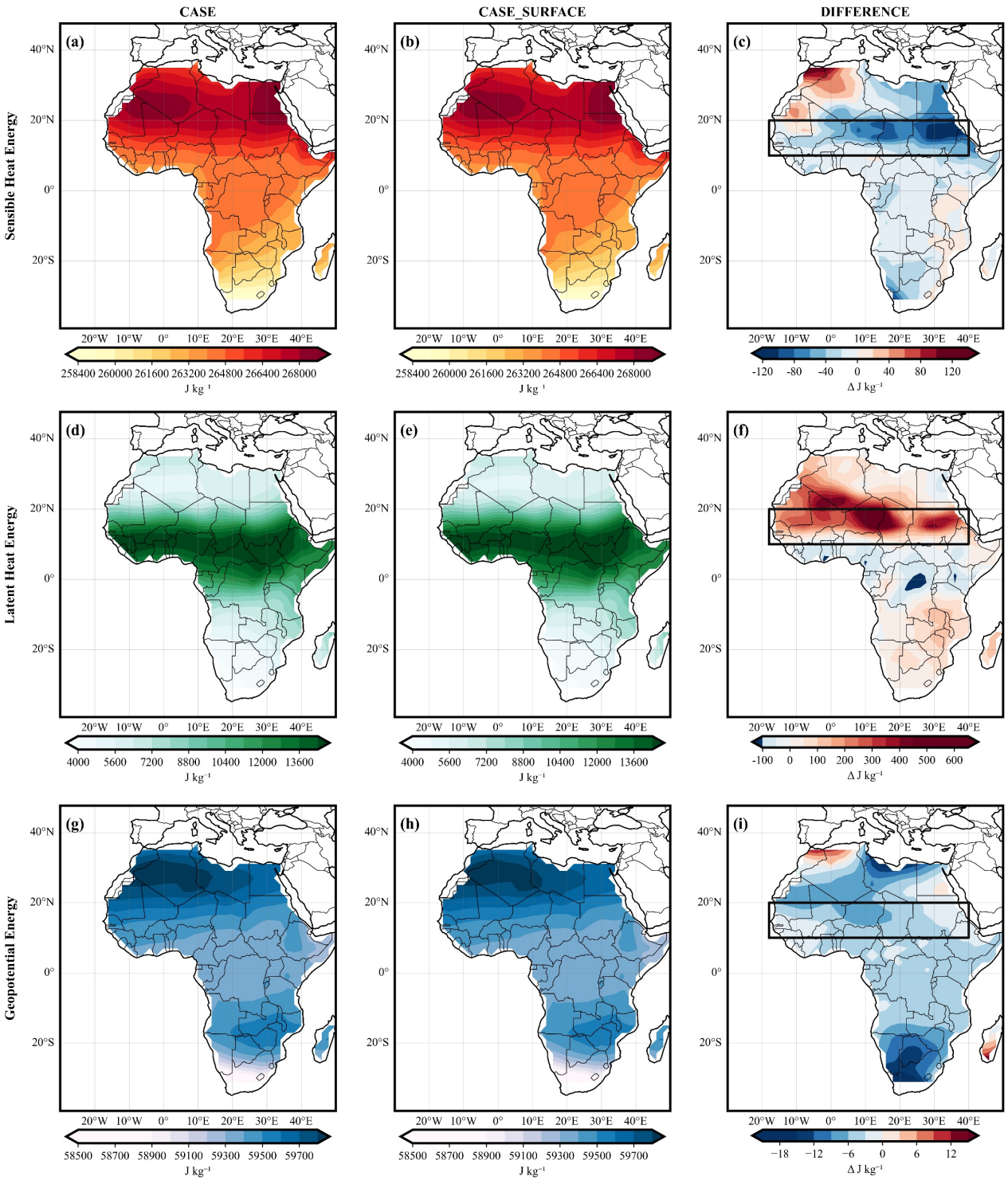

Figure 9. JJA climatology of MSE energy components over the Sahel. Panels show (a) - (c) sensible heat; (d) - (f) latent heat; and (g) - (i) geopotential energy for the Control, GGW, and Sahel greenbelt change (GGW minus change).

Increased moisture, reduction in temperature, and geopotential enhance MSE and shift energy maxima northward (Bello & Li, 2025)

Figure 9 represents the JJA climatological distribution of MSE energy compo-

nents; from these, the latent heat energy change (GGW minus Control) (**Figure 9(f)**) dominates the MSE response, driving both the amplification and northward migration of total MSE change (**Figure 2(c)**; **Figure 8(c)**). This pronounced increase in latent heat energy north of 15˚N and its poleward displacement (**Figure 9(f)**) provide the primary positive contribution to the enhancement of MSE. In contrast, sensible heat change (**Figure 9(c)**) and geopotential energy change (**Figure 9(i)**) exhibit widespread decreases over the Sahel, enhancing the total MSE by lowering surface temperature and increasing atmospheric moisture. The reduction in sensible heating (**Figure 9(c)**) weakens surface thermal contributions, while the decline in geopotential energy change (**Figure 9(i)**) reduces the gravitational component of the column energy. However, these negative contributions remain secondary to the strong moisture-driven enhancement.

Overall, the result indicates that Sahelian MSE variability is primarily moisture-controlled (**Figure 8(i)**), with latent heat changes (**Figure 9(f)**) governing the net MSE intensification and shifting northward (**Figure 2(c)**).

In the next term, we will explain the vertical profile of MSE components.

3.6. Vertical Structure of MSE Components

Figure 10 shows the vertical cross-section of MSE components along 0˚E for the control, GGW, and the green belt-induced vegetation change (GGW minus Control). Sensible heat (**Figures 10(a)-(c)**), the control (**Figure 10(a)**), exhibits an increase over the monsoon region (1000 - 850 hPa) (10˚N - 20˚N) and decreases with altitude, reflecting strong surface heating and a decrease in boundary layer humidity. The impact of the greenbelt/change/(**Figure 10(c)**) reveals a reduction in lower-tropospheric sensible heat, indicating suppressed turbulent fluxes, with minor compensation above 700 hPa, consistent with slight vertical redistribution of thermal energy. Latent heat (**Figures 10(d)-(f)**): control (**Figure 10(d)**) shows a pronounced increase in latent heat in the lower troposphere over the monsoon core, indicative of active moisture convergence and convection. The change (**Figure 10(f)**) reveals positive anomalies intensifying throughout the lower troposphere, extending northward to the Sahel, with persistent signals above 700 hPa, highlighting enhanced vertical moisture transport and amplified column-integrated MSE.

Geopotential energy (**Figures 10(g)-(i)**), in the control (**Figure 10(g)**), geopotential height decreases in the lower troposphere over the monsoon region, supporting ascent. The change (**Figure 10(i)**) produces further reduction in the lower troposphere, aligned with stronger ascent, and modest increases aloft, reflecting vertical redistribution and reinforcing convective organization (Al-Shamsi et al., 2025).

In summary, across the vertical column, greenbelt-driven vegetation restoration enhances latent heat fluxes and lower-tropospheric MSE while reducing sensible and geopotential energy. The moisture process is the dominant driver of tropospheric energy organization in the Sahel, promoting energy maxima northward.

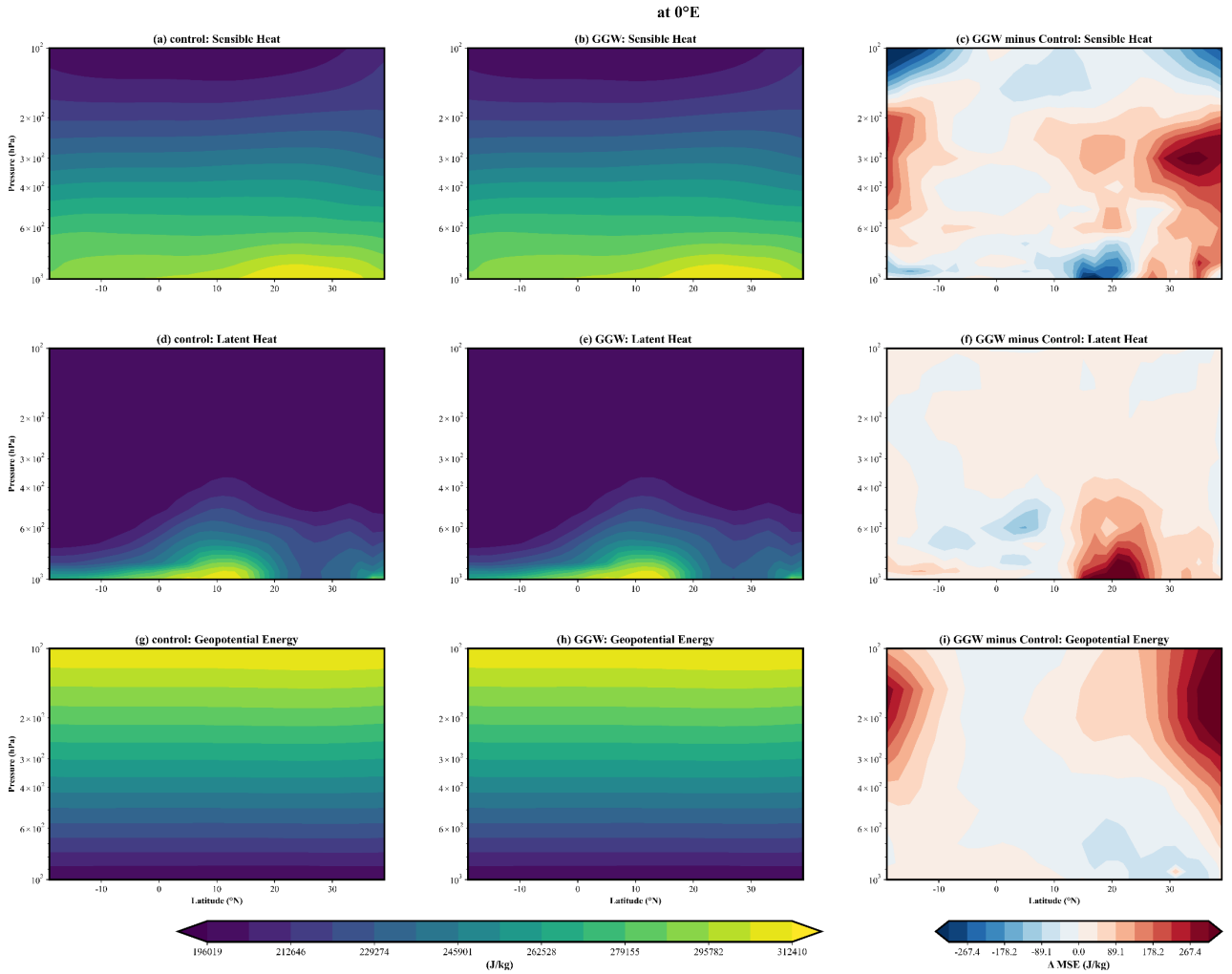

Figure 10. Vertical cross-section of JJA MSE components along 0˚E over the Sahel. Panels show sensible heat (a) - (c); latent heat (d) - (f); and geopotential energy (g) - (i) for the Control, GGW, and Sahel greenbelt induced change (GGW minus Control).

Next, we will observe the changes in MSE transport.

3.7. Vertical Structure of MSE Transport and Circulation Adjustment

Figure 11 illustrates the JJA climatological distribution of moist static energy (MSE) and winds at 850, 600, and 200 hPa, revealing vertical dynamical controls of Sahelian moist static energy.

At 850 hPa, the GGW (Figure 11(b)) reveals enhanced MSE peaks near 15˚N, fed by strengthened southwesterly moisture advection from the tropical Atlantic. Intensified northeasterly trade winds limit northward moisture penetration, which weakened MSE's northern part. The change (Figure 11(f)), stronger low-level westerlies and weakened northeasterly trade winds, reduced dry air intrusion, allowing moisture to extend farther north and east, favoring the MSE maxima northward.

At 600 hPa, the GGW (Figure 11(e)) African easterly jet flows deeper south-

ward, and the enhanced northeasterly flow promotes mid-level dry intrusion, suppressing MSE north of 12˚N. The change field (**Figure 11(f)**) northeasterly dry intrusion becomes weaker, and enhanced southwesterlies strengthen enhanced meridional moisture transport and shift the MSE core northward.

At 200 hPa, the GGW (**Figure 11(h)**) strengthened the tropical easterly jet with a core found in the eastern part, with MSE decreasing over the entire Sahel. The change field (**Figure 11(i)**) reveals that the TEJ becomes strongly retreated and weakens, as well as the northeasterly trade wind weakening; however, the MSE still decreased, implying that TEJ has an indirect role in regulating MSE (Nicholson & Klotter, 2021). Overall, Sahelian MSE variability is dominated by low-level moisture advection and vertical warm air transport, while the TEJ plays a secondary role.

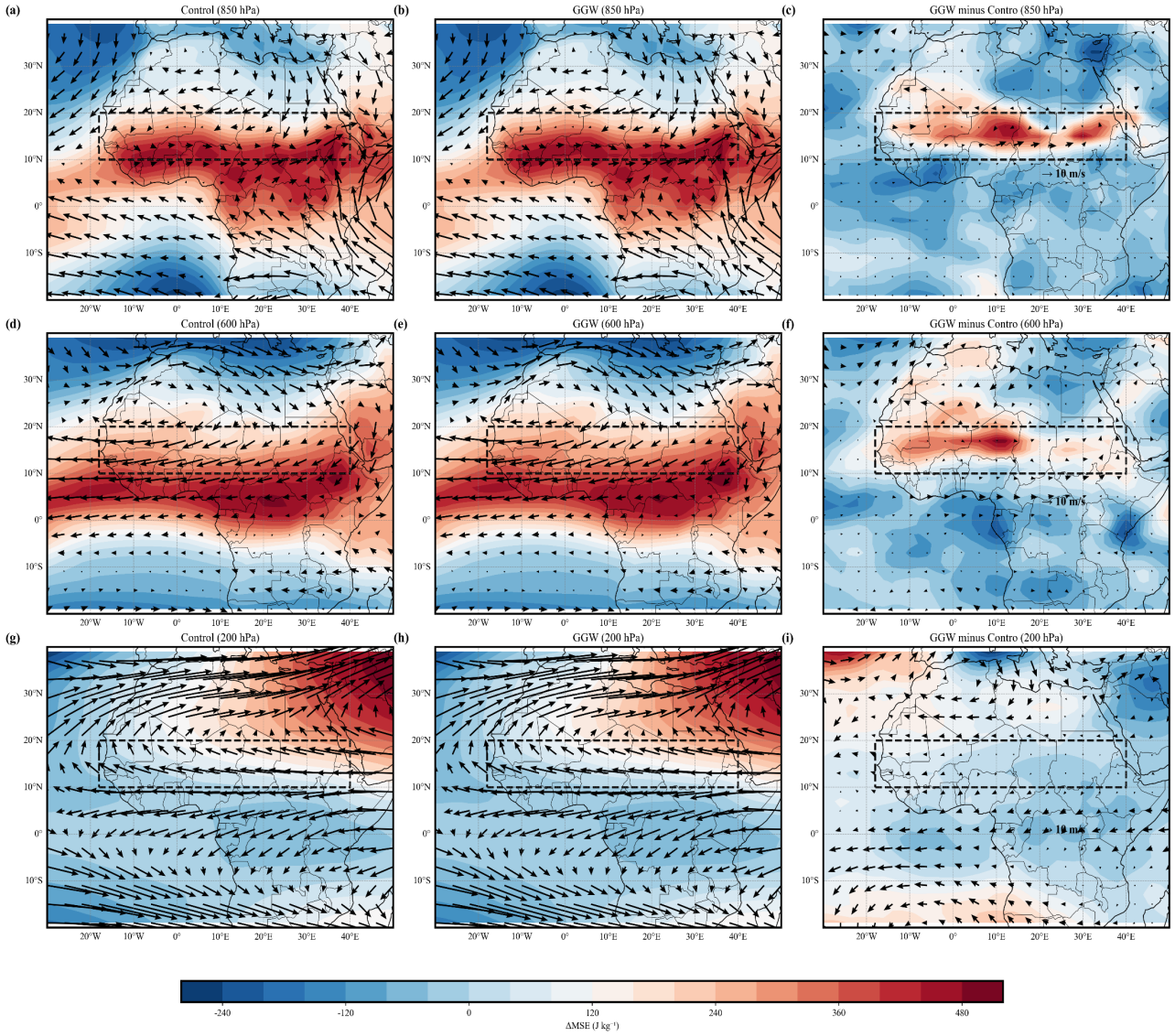

Figure 11. JJA climatological distribution of MSE and wind vectors at 850 hPa (a) - (c); 600 hPa (d) - (f) and 200 hPa (g) - (i) for Control, GGW and GGW minus Control.

3.8. Zonal-Mean Meridional Structure of MSE Components

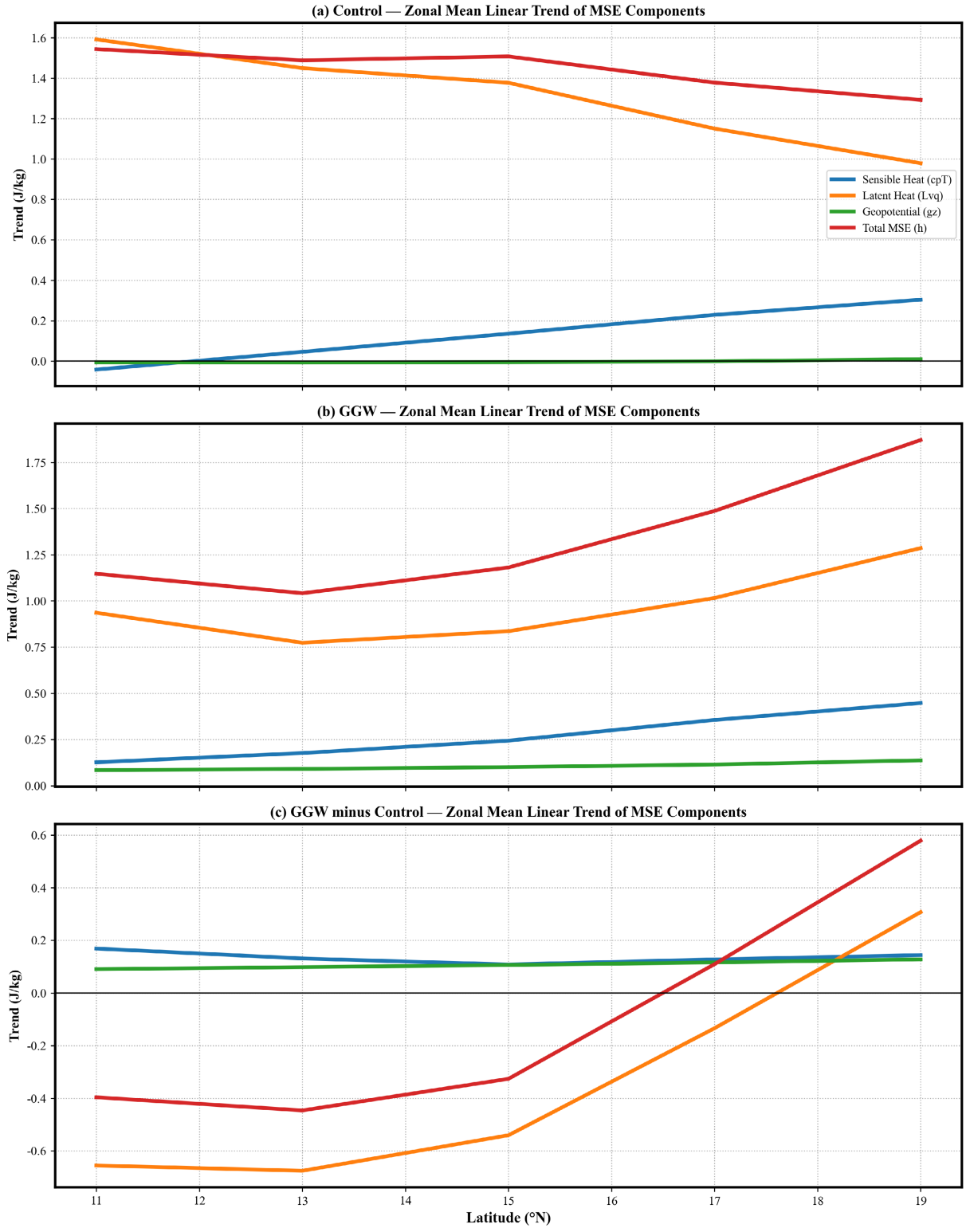

Figure 12. JJA zonal mean meridional structure of total MSE and its components over the Sahel. Panels show the climatological mean for (a) the control experiment, (b) the GGW experiment, and (c) their difference (GGW minus Control), highlighting the meridional distribution and moisture-driven amplification of MSE in response to vegetation restoration.

Figure 12 presents the JJA zonal mean meridional structure of total moist static energy (MSE) and its components. Panels (a) and (b) show the climatological means for the control and GGW experiments, respectively, while panel (c) displays their difference (GGW minus Control). In the control experiment (Figure 12(a)), the climatological zonal mean shows that total MSE and its latent heat component are higher south of 15˚N, while they are lower over North Africa. In contrast, the sensible heat and geopotential components are higher north of 15˚N. This meridional contrast indicates that thermodynamic drying and enhanced static stability dominate over North Africa, whereas moisture-driven energy increases are confined to the Sahel in the mean state. The GGW experiment (Figure 12(b)) reveals that total MSE becomes the dominant component north of 15˚N, closely followed by latent heat. Concurrently, the sensible heat and geopotential contributions weaken, implying a transition from dry static energy to moisture-dominant energy amplification.

The greenbelt-induced change (GGW minus Control, Figure 12(c)) further supports this: sensible heat and geopotential energy show negative anomalies over the northern Sahel, while total MSE and latent heat exhibit positive anomalies poleward of 15˚N. This response is primarily moisture-driven rather than dynamically forced (Dixon et al., 2013). Overall, the GGW amplifies the latent heat component of MSE, playing a dominant role in moisture and associated energy transport in modulating Sahelian thermodynamic structure.

4. Summary and Conclusion

This study demonstrates the fundamental role of the Sahel greenbelt in reorganizing regional moist static energy (MSE) and West African Monsoon energetics using 30-year equilibrium simulations from the CESM2 model. By applying a column-integrated MSE budget framework, we quantified how a 70% vegetation increase over the Sahel (10˚N - 18˚N) transforms the thermodynamic and dynamic structure of the monsoon system.

The results establish that greenbelt forcing shifts the MSE maximum poleward from 5˚N - 12˚N to 15˚N - 18˚N, increasing core values over the central Sahel from 1.254 to 1.507 $kJ \cdot kg^{-1}$ (Figure 2(c)). This northward expansion is not merely a magnitude change but represents a fundamental reorganization of monsoon energetics. The seasonal evolution (Figure 3) reveals a distinct meridional dipole during the peak monsoon. MSE decreases over the Guinea coast while increasing over North Africa, indicating energy redistribution from coastal to interior regions, with delayed moisture release extending convective potential into the post-monsoon period (Fontaine et al., 2002).

The mechanism driving this transformation operates through multiple coupled processes. First, vegetation recovery enhances evapotranspiration, increasing latent heat flux by +4.33 $W \cdot m^{-2}$ (Figure 7(e)), which repartitions surface energy from sensible to latent heat dominance. This shift moistens the boundary layer, elevates moist enthalpy, and reduces dry static stability consistent with (Hay-Chapman &

Dirmeyer, 2023; Helbig et al., 2016), who demonstrated that enhanced latent heat flux increases atmospheric wetting and moisture injection into the vertical column.

Second, the greenbelt induces fundamental circulation adjustments. Strengthened low-level westerlies transport warm, moist air from the tropical Atlantic deeper into the eastern Sahel, while reduced northeasterly dry advection minimizes dry intrusion from the Sahara (**Figure 11**). The African Easterly Jet weakens and shifts northward, favoring vertical transport of moist energy, while the Tropical Easterly Jet plays a secondary role. These circulation changes collectively enhance low-level MSE accumulation and support northward moisture penetration.

The column-integrated MSE budget (**Figure 6**) quantifies the energetic consequences. Atmospheric net energy gain increases by +7.2 $W \cdot m^{-2}$ north of 15˚N. Crucially, circulation-driven advection accounts for nearly two-thirds of this increase, with vertical advection as the dominant contributor (43%), efficiently transporting high-MSE air from the boundary layer to the free atmosphere. Mean horizontal flow exports energy (−2.53 $W \cdot m^{-2}$), partially offset by anomalous wind import (+1.29 $W \cdot m^{-2}$), demonstrating strong coupling between thermodynamic forcing and dynamic feedbacks, a hallmark of monsoon intensification (Akinsanola & Zhou, 2019).

The atmospheric energy surplus (+7.67 $W \cdot m^{-2}$) is primarily fueled by enhanced shortwave absorption (+5.73 $W \cdot m^{-2}$) and latent heat flux, partially offset by longwave cooling. This confirms that vegetation recovery enhances atmospheric energy content predominantly through moisture-driven processes rather than thermal amplification alone. The zonal mean meridional structure (**Figure 12(c)**) further confirms this moisture dominance: latent heat increases north of 15˚N while sensible and geopotential components decrease, indicating a thermodynamic regime shift from sensible heating-controlled dry boundary layer to latent heat-dominated moist regime across the northern Sahel.

In summary, these findings demonstrate that Sahel greenbelt-induced vegetation recovery reorganizes monsoon energetics through three interconnected pathways: 1) surface energy repartitioning from sensible to latent heat dominance, moistening the boundary layer; 2) circulation adjustments that strengthen moist westerly inflow while weakening dry northeasterly intrusion; and 3) dynamically reinforced vertical transport that efficiently lifts high-MSE air into the free atmosphere. Together, these processes promote northward expansion of convective energy, shifting the Sahel climate toward a wetter regime north of 15˚N.

The results provide a mechanistic foundation for evaluating large-scale reforestation as a regional climate adaptation strategy. By strengthening moisture recycling and dynamically reinforcing ascent, land restoration offers potential benefits for agriculture, water resources, and ecosystem recovery across the Sahel. However, remaining uncertainties warrant further investigation. Higher-resolution simulations with dynamic vegetation representations could better capture local-scale vegetation-atmosphere feedbacks across the Sahel's east-west gradient.

Additionally, incorporating aerosol-radiation interactions, dust feedbacks, and projected climate change-driven shifts in large-scale circulation will further refine understanding of greenbelt impacts. Strengthening integration with observational networks and in-situ flux measurements remains essential to validate these model-based insights and translate them into effective adaptation strategies for the millions who depend on the West African Monsoon's predictability.

Acknowledgements

I extend my deepest gratitude to my supervisor, Professor Jian Cao, for his unwavering support and insightful guidance throughout every step of this research. His deep commitment to academic excellence and meticulous attention to detail have significantly shaped this work.

I wish to express my sincere appreciation to my university, Nanjing University of Information Science and Technology (NUIST), for providing this golden opportunity to conduct research and for the invaluable academic platform it offers.

I am equally thankful to the Chinese students of my esteemed Professor. For their brilliant intellect, their open-minded nature, and their unwavering kindness in support, I hold profound and unwavering respect from the bottom of my heart.

We sincerely thank the reviewers for their time, careful evaluation, and constructive feedback. Their insightful comments have greatly improved the clarity, rigor, and overall quality of this manuscript.

Finally, I acknowledge with profound gratitude that God's grace has sustained my health and strength throughout this endeavor. To God, I owe my deepest thanks for the continued well-being that made this work possible.

Conflicts of Interest

The authors declare no conflicts of interest regarding the publication of this paper.

References

Adigun, T. O., Arowolo, A. V., & Balogun, I. A. (2024). Investigating the Influence of Vertical Moisture Integrated Flux Convergence on Rainfall Recovery in the Sahel Region of West Africa. *Environmental Systems Research, 13,* Article No. 60. https://doi.org/10.1186/s40068-024-00375-2

Akinsanola, A. A., & Zhou, W. (2019). Dynamic and Thermodynamic Factors Controlling Increasing Summer Monsoon Rainfall over the West African Sahel. *Climate Dynamics, 52,* 4501-4514. https://doi.org/10.1007/s00382-018-4394-x

Al-Shamsi, N., Al Kaabi, A., Al Mandous, A., Al Yazeedi, O., Al Mazrouei, A., Weston, M. et al. (2025). Synoptic-Scale Forcing and Its Role in a Rare Severe Rainfall Event over the UAE: A Case Study of 15-16 April 2024. *Atmosphere, 16,* Article 1267. https://doi.org/10.3390/atmos16111267

Baumhauer, R. (2025). The Major Regions of the Continent. In *Physical Geography of Africa* (pp. 9-15). Springer.

Bello, A. A., & Li, J. (2025). Winter Sea Surface Temperature Interhemispheric Dipole as a Predictor for Sahel Summer Rainfall. *Environmental Research Letters, 20,* Article 104033. https://doi.org/10.1088/1748-9326/ae01c0

Buontempo, C., Booth, B., & Moufouma-Okia, W. (2012). The Climate of the Sahel. In *West African Studies Global Security Risks and West Africa Development Challenges: Development Challenges* (pp. 58-72). OECD Publishing.

Chakraborty, S., Sullivan, S. C., & Feng, Z. (2023). An Overview of Mesoscale Convective Systems: Global Climatology, Satellite Observations, and Modeling Strategies. In *Clouds and Their Climatic Impacts: Radiation, Circulation, and Precipitation* (pp. 195-221). Wiley.

Danabasoglu, G., Lamarque, J. F., Bacmeister, J., Bailey, D. A., DuVivier, A. K., Edwards, J. et al. (2020). The Community Earth System Model Version 2 (CESM2). *Journal of Advances in Modeling Earth Systems, 12,* e2019MS001916. https://doi.org/10.1029/2019ms001916

Deng, A., Hao, X., & Qu, J. J. (2024). A Preliminary Assessment of Land Restoration Progress in the Great Green Wall Initiative Region Using Satellite Remote Sensing Measurements. *Remote Sensing, 16,* Article 4461. https://doi.org/10.3390/rs16234461

Diba, I., Camara, M., & Diedhiou, A. (2019). Impacts of the Sahel-Sahara Interface Reforestation on West African Climate: Intra-Annual Variability and Extreme Temperature Events. *Atmospheric and Climate Sciences, 9,* 35-61. https://doi.org/10.4236/acs.2019.91003

Diop, S., Guisse, A., Sene, C., Cisse, B., Diop, N. R., Ka, S. D. et al. (2018). Combating Desertification and Improving Local Livelihoods through the GGWI in the Sahel Region: The Example of Senegal. *Journal of Resources and Ecology, 9,* 257-265. https://doi.org/10.5814/j.issn.1674-764x.2018.03.005

Dixon, N. S., Parker, D. J., Taylor, C. M., Garcia-Carreras, L., Harris, P. P., Marsham, J. H. et al. (2013). The Effect of Background Wind on Mesoscale Circulations above Variable Soil Moisture in the Sahel. *Quarterly Journal of the Royal Meteorological Society, 139,* 1009-1024. https://doi.org/10.1002/qj.2012

Djakouré, S., Amouin, J., Kouadio, K. Y., & Kacou, M. (2024). Mesoscale Convective Systems and Extreme Precipitation on the West African Coast Linked to Ocean-Atmosphere Conditions during the Monsoon Period in the Gulf of Guinea. *Atmosphere, 15,* Article 194. https://doi.org/10.3390/atmos15020194

Fontaine, B., Philippon, N., Trzaska, S., & Roucou, P. (2002). Spring to Summer Changes in the West African Monsoon through NCEP/NCAR Reanalyses (1968-1998). *Journal of Geophysical Research: Atmospheres, 107,* ACL 1-1-ACL 1-9. https://doi.org/10.1029/2001jd000834

Garric, G., Douville, H., & Déqué, M. (2002). Prospects for Improved Seasonal Predictions of Monsoon Precipitation over Sahel. *International Journal of Climatology, 22,* 331-345. https://doi.org/10.1002/joc.736

Geremew, T., Ullah, I., Akinsanola, A. A., Muleta, D., Teshome, F., Syed, S. et al. (2025). Unravelling Southern Ocean Sea Surface Temperatures Impacts on Long Rainfall Variability in East Africa. *Atmospheric Research, 327,* Article 108406. https://doi.org/10.1016/j.atmosres.2025.108406

Grove, A. T. (1978). Geographical Introduction to the Sahel. *The Geographical Journal, 144,* 407-415. https://doi.org/10.2307/634817

Hay-Chapman, F. M., & Dirmeyer, P. A. (2023). A Novel Method for Diagnosing Land-Atmosphere Coupling Sensitivity in a Single-Column Model. *Journal of Hydrometeorology, 24,* 2207-2223. https://doi.org/10.1175/jhm-d-22-0237.1

Helbig, M., Wischnewski, K., Kljun, N., Chasmer, L. E., Quinton, W. L., Detto, M. et al. (2016). Regional Atmospheric Cooling and Wetting Effect of Permafrost Thaw-Induced Boreal Forest Loss. *Global Change Biology, 22,* 4048-4066. https://doi.org/10.1111/gcb.13348

Hiernaux, P., Diawara, M. O., Kergoat, L., & Mougin, É. (2015). La contrainte fourragère des élevages pastoraux et agro-pastoraux du Sahel. In *Book: Les Sociétés Rurales Face*

Aux Changements Climatiques et Environnementaux en Afrique de l'Ouest (pp. 171-191). IRD Éditions Books.

Hill, S. (2020). Forced Monsoon Rainfall Changes and the Moist Static Energy Budget: The Sahel and Elsewhere. In *EGU General Assembly Conference Abstracts*. European Geosciences Union.

Hill, S. A. (2016). *Energetic and Hydrological Responses of Hadley Circulations and the African Sahel to Sea Surface Temperature Perturbations*. Ph.D. Thesis, Princeton University.

Hill, S. A., Ming, Y., Held, I. M., & Zhao, M. (2017). A Moist Static Energy Budget-Based Analysis of the Sahel Rainfall Response to Uniform Oceanic Warming. *Journal of Climate, 30,* 5637-5660. https://doi.org/10.1175/jcli-d-16-0785.1

Ingrosso, R., & Pausata, F. S. R. (2024). Contrasting Consequences of the Great Green Wall: Easing Aridity While Increasing Heat Extremes. *One Earth, 7,* 455-472. https://doi.org/10.1016/j.oneear.2024.01.017

Inoue, K., Kelley, M., Fridlind, A. M., Biasutti, M., & Elsaesser, G. S. (2025). *Accurate Column Moist Static Energy Budget in Climate Models. Part 1: Conservation Equation Formulation, Methodology, and Primary Results Demonstrated Using GISS Model E3*. https://arxiv.org/abs/2407.13855

Joly, F. (2021). Aridity. In *Mankind and Deserts 1: Deserts, Aridity, Exploration and Conquests* (pp. 65-149). Wiley.

Kaagita, V., Thandlam, V., Sakirevu Palli, V. R., Muriki, S. K., & Mathew, M. (2024). Diagnosing the Role of Atmospheric Variability on the Extreme Summer Monsoon Precipitation Events over India. *Discover Atmosphere, 2,* Article No. 19. https://doi.org/10.1007/s44292-024-00021-7

Kebe, I., Diallo, I., Sylla, M. B., De Sales, F., & Diedhiou, A. (2020). Late 21st Century Projected Changes in the Relationship between Precipitation, African Easterly Jet, and African Easterly Waves. *Atmosphere, 11,* Article 353. https://doi.org/10.3390/atmos11040353

Kenfack, K., Djiotang Tchotchou, L. A., Marra, F., Bellomo, K., Tamoffo, A. T., Tchana, B. C. et al. (2025). Radiative Anomalies Associated with Extreme Precipitation of November 2023 in Equatorial Central Africa. *Atmospheric Research, 321,* Article 108090. https://doi.org/10.1016/j.atmosres.2025.108090

Kenfack, K., Marra, F., Djomou, Z. Y., Tchotchou, L. A. D., Tamoffo, A. T., & Vondou, D. A. (2024). Dynamic and Thermodynamic Contribution to the October 2019 Exceptional Rainfall in Western Central Africa. *Weather and Climate Dynamics, 5,* 1457-1472. https://doi.org/10.5194/wcd-5-1457-2024

Kirk, D. J. (2024). *Case Study in Observing the Vegetation-Albedo Feedback during Climate Change in the Sahel*. Lund University Publications.

Lawrence, D. M., Fisher, R. A., Koven, C. D., Oleson, K. W., Swenson, S. C., Bonan, G. et al. (2019). The Community Land Model Version 5: Description of New Features, Benchmarking, and Impact of Forcing Uncertainty. *Journal of Advances in Modeling Earth Systems, 11,* 4245-4287. https://doi.org/10.1029/2018ms001583

Li, T., & Hu, F. (2019). A Coupled Moisture-Dynamics Model of the Madden-Julian Oscillation: Convection Interaction with First and Second Baroclinic Modes and Planetary Boundary Layer. *Climate Dynamics, 53,* 5529-5546. https://doi.org/10.1007/s00382-019-04879-x

Li, Z., Chen, J., Wang, C., Wang, W., Fu, Y., Chen, X. et al. (2025). Enhancing Sustainable Urban Environments in China: Daytime Radiative Cooling for Building Energy Efficiency and Heat Island Mitigation. *Applied Energy, 393,* Article 126138.

https://doi.org/10.1016/j.apenergy.2025.126138

Mbow, C. (2017). *The Great Green Wall in the Sahe*. https://api.semanticscholar.org/CorpusID:134487889

McGregor, G. (2024). Surface Atmosphere Interactions and Heatwaves. In *Heatwaves: Causes, Consequences and Responses* (pp. 261-304). Springer.

Mechiche-Alami, A., O'Byrne, D., Tengberg, A., & Olsson, L. (2022). Evaluating the Scaling Potential of Sustainable Land Management Projects in the Sahelian Great Green Wall Countries. *Environmental Research Letters, 17,* Article 084016. https://doi.org/10.1088/1748-9326/ac8111

Meng, X., Dong, G., & Fenetahun, Y. (2025). Forecasting Sub-Pixel Vegetation Potential Shifts to Guide Restoration Planning for the African Great Green Wall. *GIScience & Remote Sensing, 62,* Article 2574730. https://doi.org/10.1080/15481603.2025.2574730

Miller, R. L., Slingo, A., Barnard, J. C., & Kassianov, E. (2009). Seasonal Contrast in the Surface Energy Balance of the Sahel. *Journal of Geophysical Research: Atmospheres, 114,* Article 129165555. https://doi.org/10.1029/2008jd010521

Monerie, P. A., Mohino, E., Moine, M. P., Biasutti, M., Pohl, B., & Mignot, J. (2025). Exploring Uncertainty in Dynamical Future Changes in Sahel Precipitation: The Extratropical Influence. *Climate Dynamics, 63,* Article No. 353. https://doi.org/10.1007/s00382-025-07835-0

Nicholson, S. E., & Klotter, D. (2021). The Tropical Easterly Jet over Africa, Its Representation in Six Reanalysis Products, and Its Association with Sahel Rainfall. *International Journal of Climatology, 41,* 328-347. https://doi.org/10.1002/joc.6623

Oueslati, B., Camberlin, P., Zoungrana, J., Roucou, P., & Diallo, S. (2018). Variability and Trends of Wet Season Temperature in the Sudano-Sahelian Zone and Relationships with Precipitation. *Climate Dynamics, 50,* 1067-1090. https://doi.org/10.1007/s00382-017-3661-6

Raj, J., Bangalath, H. K., & Stenchikov, G. (2019). West African Monsoon: Current State and Future Projections in a High-Resolution AGCM. *Climate Dynamics, 52,* 6441-6461. https://doi.org/10.1007/s00382-018-4522-7

Rodríguez-Fonseca, B., Mohino, E., Mechoso, C. R., Caminade, C., Biasutti, M., Gaetani, M. et al. (2015). Variability and Predictability of West African Droughts: A Review on the Role of Sea Surface Temperature Anomalies. *Journal of Climate, 28,* 4034-4060. https://doi.org/10.1175/jcli-d-14-00130.1

Sabut, A., & Mishra, A. (2026). A Century of Drought Research (1900-2023): Scientific Developments, Methodological Innovations, and Emerging Frontiers. *Water Resources Research, 62,* e2025WR041987. https://doi.org/10.1029/2025wr041987

Saley, I. A., Salack, S., Sanda, I. S., Moussa, M. S., Bonkaney, A. L., Ly, M. et al. (2019). The Possible Role of the Sahel Greenbelt on the Occurrence of Climate Extremes over the West African Sahel. *Atmospheric Science Letters, 20,* e927. https://doi.org/10.1002/asl.927

Sheen, K. L., Smith, D. M., Dunstone, N. J., Eade, R., Rowell, D. P., & Vellinga, M. (2017). Skillful Prediction of Sahel Summer Rainfall on Inter-Annual and Multi-Year Timescales. *Nature Communications, 8,* Article No. 14966. https://doi.org/10.1038/ncomms14966

Sian, K. T. C., Ayugi, B. O., Onyutha, C., Sagero, P., & Ait Brahim, Y. (2025). Rainfall Variability across Africa. In *Climate Change and Rainfall Extremes in Africa* (pp. 3-26). Elsevier. https://doi.org/10.1016/b978-0-443-28867-8.00001-0

Singh, R., & Sandeep, S. (2024). A Mechanism for the Summer Monsoon Precipitation Variability over Northwest India Driven by Moisture Deficit Transport. *Journal of Geophys-*

ical Research: Atmospheres, 129, e2023JD040180. https://doi.org/10.1029/2023jd040180

Sun, J., Yang, K., He, X., Wang, G., Wang, Y., Yu, Y. et al. (2025). Causal Pathways Underlying Global Soil Moisture-Precipitation Coupling. *Nature Communications, 16,* Article No. 8935. https://doi.org/10.1038/s41467-025-63999-7

Trench, P., Rowley, J., Diarra, M., Sano, F., & Keita, B. (2007). *Beyond Any Drought—Root Causes of Chronic Vulnerability in the Sahel.* The Sahel Working Group.

Verhoef, A., Allen, S. J., & Lloyd, C. R. (1999). Seasonal Variation of Surface Energy Balance over Two Sahelian Surfaces. *International Journal of Climatology, 19,* 1267-1277. https://doi.org/10.1002/(sici)1097-0088(199909)19:11<1267::aid-joc418>3.0.co;2-s

Wall, G. G. (2024). The Great Green Wall. *Donors.* https://Ggwobservatory.Org/En/Donors/

Xue, Y., De Sales, F., Lau, W. K., Boone, A., Feng, J., Dirmeyer, P. et al. (2010). Intercomparison and Analyses of the Climatology of the West African Monsoon in the West African Monsoon Modeling and Evaluation Project (WAMME) First Model Intercomparison Experiment. *Climate Dynamics, 35,* 3-27. https://doi.org/10.1007/s00382-010-0778-2

Yohannes, T., Yu, J., Jonah, K., Oo, K. T., Muleta, D., Adem, K. et al. (2024). A Bibliographic Review on Anthropogenic Climate Change and Drought. *Environmental Science & Policy, 160,* Article 103830. https://doi.org/10.1016/j.envsci.2024.103830

Yu, Y., Notaro, M., Wang, F., Mao, J., Shi, X., & Wei, Y. (2017). Observed Positive Vegetation-Rainfall Feedbacks in the Sahel Dominated by a Moisture Recycling Mechanism. *Nature Communications, 8,* Article No. 1873. https://doi.org/10.1038/s41467-017-02021-1

Zhao, S. (2023). *Environmental Controls on African Rainfall Variability*. Ph.D. Thesis, The University of Texas at Austin.

Zhi, Y., Li, X., Shen, T., Metternicht, G., Grainger, A., Pan, Y. et al. (2025). Land Productivity Declines in the GGW While Human Contributions to Restoration Far Outweighing Degradation. *Scientific Reports, 15,* Article No. 34948. https://doi.org/10.1038/s41598-025-18963-2